

# Deep Learning-based Accelerated MR Cholangiopancreatography without Fully-sampled Data

Jinho Kim<sup>1,2</sup>, Marcel Dominik Nickel<sup>2</sup>, and Florian Knoll<sup>1,3</sup>

<sup>1</sup>Artificial Intelligence in Biomedical Engineering, Friedrich-Alexander-Universität Erlangen-Nürnberg, Germany, <sup>2</sup>MR Application Predevelopment, Siemens Healthineers AG, Forchheim, Germany, <sup>3</sup>Center for Advanced Imaging Innovation and Research (CAI<sup>2</sup>R), Department of Radiology, New York University Grossman School of Medicine, New York, NY, USA

## Abstract

The purpose of this study was to accelerate MR cholangiopancreatography (MRCP) acquisitions using deep learning-based (DL) reconstruction at 3T and 0.55T. A total of 35 healthy volunteers underwent conventional two-fold accelerated MRCP scans at field strengths of 3T and 0.55T. We trained DL reconstructions using two different training strategies, supervised (SV) and self-supervised (SSV), with retrospectively six-fold undersampled data obtained at 3T. We then evaluated the DL reconstructions against standard techniques, parallel imaging (PI) and compressed sensing (CS), focusing on peak signal-to-noise ratio (PSNR) and structural similarity (SSIM) as metrics. We also tested DL reconstructions in a prospectively accelerated scenario to reflect real-world clinical applications and evaluated their adaptability to MRCP at 0.55T. Both DL reconstructions demonstrated a remarkable reduction in average acquisition time from 599/542 to 255/180 seconds for MRCP at 3T/0.55T. In both retrospective and prospective undersampling scenarios, PSNR and SSIM of DL reconstructions were higher than those of PI and CS. At the same time, DL reconstructions preserved the image quality of undersampled data, including sharpness and the visibility of hepatobiliary ducts. In addition, both DL approaches produced high-quality reconstructions at 0.55T. In summary, DL reconstructions trained for highly accelerated MRCP enabled a reduction in acquisition time by a factor of 2.4/3.0 at 3T/0.55T while maintaining the image quality of conventional acquisition.

## KEYWORDS

Magnetic resonance cholangiopancreatography, image reconstruction, accelerated reconstruction, Deep Learning, supervised training, self-supervised training,

## Introduction

Magnetic resonance cholangiopancreatography (MRCP) is a non-invasive imaging technique used for diagnosing diseases of the hepatobiliary system, providing detailed views of the ductal structures and related pathologies [1], [2], [3], [4]]. Initially performed using 2-D thick-slice acquisitions, MRCP has evolved into 3-D imaging, improving image quality and providing comprehensive multidimensional views. However, these improvements have resulted in longer acquisition times and are prone to motion artifacts [5]. There are two acquisition methods to address these challenges: breath-hold and triggered free-breathing. Due to the limitations of breath-holding, the triggered free-breathing acquisition method is more practical in clinical applications.

Triggered techniques allow patients to breathe naturally during the scan while minimizing motion artifacts caused by breathing. The prospective acquisition correction (PACE) technique has significantly enhanced the quality of triggered free-breathing 3-D MRCP. Compared to conventional respiratory-based triggering methods, PACE triggering produces fewer motion artifacts and provides sharper anatomical contours [6]. Furthermore, Asbach et al. [7] highlighted that PACE-triggered free-breathing 3-D MRCP (PACE-MRCP) significantly improves the visualization of hepatobiliary and pancreatic ductal structures compared to breath-holding 3-D MRCP, providing more detailed images and greater patient comfort during the scan. Despite these advantages, PACE-MRCP may require long acquisition times due to irregular breathing patterns.

To address the challenge of long acquisition times in PACE-MRCP, recent studies have focused on accelerating  $k$ -space data acquisition [8]. This acceleration is typically achieved by undersampling the  $k$ -space data, which reduces acquisition time but increases the risk of aliasing artifacts. Various reconstruction methods, such as parallel imaging (PI) and compressed sensing (CS), have been developed to address these artifacts [9], [10]]. PI significantly reduces scan time by exploiting correlations between multiple coil sensitivity profiles [11]. CS leverages the incoherence of undersampling patterns, leading to uncorrelated aliasing artifacts, and enables image reconstruction from highly undersampled and sparse  $k$ -space data [12].

In recent years, deep learning-based (DL) methods have gained popularity in MR reconstruction [13], particularly in physical model-driven DL approaches. These methods are inspired by traditional iterative optimization problems and use unrolled network architectures. Model parameters are typically determined through supervised training for prospective use on unseen data. The overall models can be viewed as generalized functions mapping undersampled data to high quality reconstructions. These methods have shown remarkable performance for the reconstruction of highly accelerated MRI [14], [15]. Despite their successes, directly applying supervised training to MRCP is challenging since it is not possible to acquire fully sampled ground truth data.

Aggarwal et al. [14] introduced a supervised DL reconstruction method (SV) that requires fully sampled ground truth, but obtaining such data, particularly for MRCP, is challenging. To address this limitation, Yamman et al. [15] proposed a self-supervised DL reconstruction method (SSV) that circumvents the need for fully sampled data. However, given the common use of accelerated MRCP in clinical settings, it is possible to train SV using moderately accelerated MRCP acquisitions as substitutes for fully sampled data. Moreover, it remains unclear whether synthesized ground truth data using conventional parallel imaging or self-supervised training is the better choice. Therefore, it is worth to compare SV and SSV in the context of accelerated MRCP.

The generalization of DL reconstruction models is a field of high relevance, as it determines the range of validity and the requirements for training data. First work investigates the domain shift between field strengths, which causes different signal-to-noise ratio (SNR) levels in reconstructions [16]. With the re-introduction of low-field MRI and its intrinsically reduced SNR levels [17], DL-enhanced image generation is also highly relevant in the context of 3-D MRCP, as it may significantly improve image quality and help to close the gap to established field strengths.

This study aims to reduce acquisition time for PACE-MRCP while preserving image quality, especially the intricate details of the hepatobiliary and pancreatic ductal structures. We perform this study using retrospective data and extend it to the prospective setting to reflect real-world clinical applications. In addition, we evaluate the generalization of DL reconstructions across different field strengths for both retrospective and prospective undersampling in PACE-MRCP.

## Theory

### MRI Reconstruction

The MRI reconstruction model can be expressed as

$$y = \mathbf{E}x + n, \tag{1}$$

where  $x$  is the final image to be recovered,  $y$  the acquired multi-coil  $k$ -space data, and  $n$  the noise. The linear encoding operator  $\mathbf{E}$  includes the coil sensitivity map matrix, the Fourier transform operator and the undersampling matrix. In general, the reconstruction of accelerated MRI is an ill-posed problem, and the solution can be obtained by incorporating regularizers that provide prior information to the objective reconstruction function. Then, the regularized optimization problem can be formulated as

$$\operatorname{argmin}_x \|y - \mathbf{E}x\|_2^2 + \lambda \mathcal{R}(x), \tag{2}$$

where  $\mathcal{R}$  is a regularization operator, and  $\lambda > 0$  is a regularization parameter to balance the data fidelity and the regularization term. Classical choices of  $\mathcal{R}$  include the  $\ell_1$ -norm of wavelet coefficients [ [12], [18]] and the  $\ell_2$ -norm of intermediate reconstructions [19].

DL reconstruction can be motivated as an unrolled gradient decent algorithm of Equation ( 2 ) with a fixed number of iterations [20]. Then the neural network is identified as derivative of the regularizer  $\mathcal{R}$  and a gradient descent step given by

$$x^{i+1} = \operatorname{argmin}_x \|y - \mathbf{E}x\|_2^2 + \lambda \|x - \mathcal{N}_\theta(x^i)\|_2^2, \tag{3}$$

where  $x^0$  is the initial reconstruction of the zero-filled  $k$ -space data and  $\mathcal{N}_\theta$  the output of the neural network parameterized with  $\theta$ . Equation ( 3 ) has a closed-form solution and it can be solved by the normal equations,

$$x^{i+1} = (E^H E + \lambda I)^{-1} (E^H y + \lambda \mathcal{N}_\theta(x^i)), \quad (4)$$

where  $I$  is the identity operator and  $E^H$  is the conjugate transpose operator of  $E$ .

## Training Manners of Deep Learning-based MRI Reconstruction

### Supervised Learning

In a supervised training manner, the DL reconstruction model is trained with training data  $\{(x_{ref}^i, y^i) : i = 0, \dots, M - 1\}$ , where  $M$  denotes the number of training data,  $x_{ref}^i$  and  $y^i$  are the coil-combined ground truth image and the multi-coil undersampled  $k$ -space data at the  $i$ -th pair, respectively. In general, while  $x_{ref}^i$  is typically a fully-sampled reconstruction, in the case of MRCP, it can be GRAPPA [21] reconstruction of two-fold data. DL reconstruction for supervised learning can be expressed as

$$\operatorname{argmin}_\theta \frac{1}{M} \sum_{i=0}^{M-1} \mathcal{L}(x_{ref}^i, f(y^i, \mathbf{E}^i; \theta)), \quad (5)$$

where  $f(y^i, \mathbf{E}^i; \theta)$  denotes the output of the unrolled network that is parameterized by  $\theta$ , and  $\mathcal{L}(\dots)$  the loss function between the ground truth and the network output. Thus, the network learns the model parameters  $\theta$  using  $x_{ref}^i$  to minimize the average loss over the full set of training data. One choice for the loss function is the mean square error loss [14].

### Self-supervised Learning

Since the acquisition of fully-sampled reconstructions is not trivial or impossible in many medical conditions, due to the long scan time, training the model in a self-supervised manner can be an alternative. The SSDU (self-supervised learning via data undersampling) [15] splits the undersampled  $k$ -space data into two subsets for training and loss calculation as

$$\Omega = \Theta \cup \Lambda, \quad (6)$$

where the undersampled data indices  $\Omega$  include both data index subsets of  $\Theta$  and  $\Lambda$ , being disjoint from  $\Theta$  and  $\Lambda$ . Then, the MRI reconstruction can be expressed as

$$\operatorname{argmin}_\theta \frac{1}{M} \sum_{i=0}^M \mathcal{L}(y_\Lambda^i, \mathbf{E}_\Lambda^i (f(y_\Theta^i, \mathbf{E}_\Theta^i; \theta))), \quad (7)$$

where  $f(y_\Theta^i, \mathbf{E}_\Theta^i; \theta)$  is the unrolled network output image using  $k$ -space data only at  $\Theta$  indices. Then, the output image is transformed into  $k$ -space data using the encoding operator  $\mathbf{E}_\Theta^i$ , specified by the  $\Lambda$  indices. SSDU defines the loss function as the combination of  $\ell_1$ - $\ell_2$  norm that is calculated between the subset  $y_\Lambda^i$  and the output  $k$ -space at  $\Lambda$  locations.

## Materials and Methods

### MRCP Data Acquisition

From February 2023 to February 2024, we collected MRCP data from 35 healthy volunteers (23 males and 12 females). All participants received an informed consent discussion and gave their written informed consent for their data being further used and processed. The mean age of the participants was 56.7, ranging from 20 to 81. Thirty-one out of the 35 volunteers were scanned at a field strength of 3T (MAGNETOM Vida and Lumina, Siemens Healthineers, Erlangen, Germany), and four volunteers at a field strength of 0.55T (MAGNETOM Free.Max, Siemens Healthineers, Erlangen, Germany). We employed multi-channel coil arrays for imaging, consisting of an 18-/12-/9-channel body array and a 36-/24-/6-channel spine array, for the Vida (3T), Lumina (3T), and Free.Max (0.55T) scanners. The volunteers were positioned in the supine, head-first orientation during the scan. We acquired 3-D MRCP data using a 3-D T2-weighted turbo spin-echo sequence (SPACE) [22] in free-breathing, using the PACE triggering method for motion management. We averaged MR signals for 1.4 and 2 times for 3T and 0.55T scanner systems, respectively, to compensate the free induction decay (FID) artifacts, as commonly done for the SPACE sequence [23]. Furthermore, we accelerated MRCP acquisition by factors of R=2 and R=6 along the phase encoding direction (fully-sampled in the read out and slice directions) with 24 autocalibration signal lines for both acceleration rates. Notably, we performed multiple scans of volunteers for the training dataset by varying the field-of-view. Table 1 shows detailed scan parameters.

### Raw Data Processing

We completed the conversion of the raw data to the ISMRMRD format [24] using the ISMRMRD<sup>1</sup> Python toolbox. We converted 3-D  $k$ -space data to a 2-D format by applying an Inverse Fourier Transform (IFT) along the fully-sampled slice (partition) direction. We performed a volume-wise normalization on the stack of 2-D  $k$ -space data to ensure consistent data scaling across volumes. Then, we undersampled the initial two-fold accelerated MRCP data by an additional factor of three to generate the six-fold undersampled input for training the network.

Furthermore, we estimated coil sensitivity maps using the ESPIRiT algorithm [25] as part of our preliminary steps using the Sigpy Python package [26] with a  $24 \times 24$  fully-sampled center  $k$ -space block and a  $5 \times 5$  kernel. Contrary to the default parameter in Sigpy, we did not crop the background to zero in the image domain. We maintained consistency across all reconstructions in this study by using the same predefined coil sensitivity maps.

### Deep Learning-based Reconstruction

#### Dataset Preparation

We divided our group of 35 volunteers into three independent sets for the study. The training and validation datasets included 18 volunteers and four volunteers, respectively, all scanned at 3T and using six-fold retrospective undersampling. Due to multiple scans of volunteers in the training dataset, the training dataset included 39 data volumes. Retrospectively and prospectively undersampled data with an acceleration factor of R=6 were collected from the remaining 13 volunteers, with nine scanned at 3T and four at 0.55T. The test dataset included these data. Fully-sampled ground truth data were obtained from the R=2 data using ESPIRiT-based coil-combined GRAPPA [21].

---

<sup>1</sup> <https://pypi.org/project/ismrmrd/>

## Network Architectures

We built a ResNet [27]-based DL reconstruction model for SV [14] and SSV [15]. For SV, we used zero-filled multi-coil  $k$ -space from retrospective undersampling of R=6 as the input and the GRAPPA reconstruction of R=2 as the reference for training. For SSV, the retrospective R=6 undersampling,  $\Omega$ , was further split into two mutually exclusive subsets,  $\Theta$  for the input and  $\Lambda$  for the reference. The subsets  $\Theta$  and  $\Lambda$  were sampled in a 1-D Gaussian distribution to match the aliasing distribution of  $\Omega$  [28]. We employed pre-estimated coil sensitivity maps [25] to train both models. Both trainings used the same DL model, which contained 12 unrolling steps and shared model weights over the steps. Each unrolling step consisted of eight residual blocks. We used the Adam optimizer with a learning rate of 0.0003 and minimized  $\ell_1$ - $\ell_2$  loss [15] in the  $k$ -space domain for both SV and SSV.

## Conventional Reconstruction

As reference reconstructions, iterative parallel imaging (CG-SENSE) [19] and compressed sensing (CS) [12] based on the Sigpy Python package [26] were used. Through empirical testing, we determined that the optimal regularization parameters for balancing SNR and aliasing artifacts were 0.01 for CG-SENSE and 0.008 for CS, respectively.

## Evaluation

We assessed two DL models through quantitative and qualitative comparisons with CG-SENSE and CS. In the retrospective study, we computed average peak signal-to-noise ratio (PSNR) and structural similarity (SSIM) metrics for the test dataset. These metrics were computed on the magnitude-valued 3-D reconstruction volume, specifically the stack of the absolute-valued 2-D reconstructions.

Reconstructions, including CG-SENSE, CS, SSV, and SV, on retrospective undersampling at R=6 were compared to the GRAPPA reconstruction at R=2. We also calculated the average PSNR and SSIM over 13 test datasets, nine for 3T and four for 0.55T. A paired t-Test was performed to prove statistical significance of DL models against reconstructions in the comparison group in terms of PSNR and SSIM. A  $p$ -value of less than 0.05 was considered statistically significant. In the prospective study, we focused on perceptual image quality.

In addition, we obtained line profiles from reconstructions to analyze details of the hepatobiliary ducts, gallbladder as well as aliasing artifacts. The line profiles were manually selected based on the maximum intensity projection (MIP) image of the 3-D reconstructed volume. Moreover, we calculated the Pearson product-moment correlation coefficient (PPMCC) [29] of the line profiles for all reconstructions with respect to the GRAPPA reconstruction at R=2. The PPMCC serves as a measure of similarity, with values closer to one indicating a higher degree of similarity between two profiles.

## Hardware and Tools

All experiments were conducted on a system equipped with an AMD Rome 7662 CPU 2.0 GHz, 512 GB of RAM, and an NVIDIA Tesla A100 SXM4 with 40 GB memory. Our model development was performed on a Linux Ubuntu v20.04.6 LTS environment, with Python v3.10.14, PyTorch v2.1.2, CUDA v11.8.0, PyTorch Lightning v2.2.5, and Sigpy v0.1.26.

## Results

### Retrospective study

Figure 1 depicts reconstructions for retrospective undersampling with R=6 at 3T and 0.55T, along with PSNR and SSIM metrics related to GRAPPA reconstruction at R=2. The top row of each subfigure presents MIP views. The red boxes on the MIP images determine the view of the cropped MIP images in the second row. The last row shows representative slices depicting differences in interesting anatomical details. Note that the metrics are calculated on 3-D volumes, not on MIP images. In Figure 1(a), which includes results from the 3T scanners, CG-SENSE achieves PSNR (dB)/SSIM (%) values of 35.32/75.64, while CS, SSV, and SV show values of 38.83/82.46, 39.67/82.85, and 40.34/85.50, respectively. In addition, the blue circles in Figure 1(a) illustrate that DL reconstructions remove aliasing artifacts, which conventional reconstructions struggle with. Furthermore, the orange circles in Figure 1(a) indicate that DL reconstructions preserve the sharpness of the common bile duct. In Figure 1(b), showing 0.55T results, CS-SENSE achieves PSNR (dB)/SSIM (%) values of 23.58/28.77, CS 30.38/59.20, SSV 31.71/69.93, and SV 32.17/71.41. The turquoise circles in Figure 1(b) demonstrate that DL reconstructions efficiently suppress background noise while presenting hepatobiliary ducts.

Figure 2 contains violin plots of PSNR in dB and SSIM in % for the two employed field strengths. These metric scores are derived from nine volunteers at 3T and four volunteers at 0.55T in the test dataset. DL reconstructions consistently outperform conventional reconstructions. In particular, SV achieves the highest median values for both PSNR and SSIM metrics, with SSV and CS closely following, though with slightly lower metric scores. CG-SENSE consistently performs the worst across all experiments. Table 2 summarizes the average PSNR and SSIM of the test dataset, along with the corresponding *p*-values at 3T and 0.55T. SV consistently achieves the highest metrics for both field strengths. Therefore, the other reconstruction methods are compared to SV for a t-Test. The t-Test results show statistical significance between SV and CG-SENSE, with all *p*-values below 0.05. Although SV is statistically significant compared to CS in terms of SSIM at 0.55T, it does not show statistical significance over CS and SSV in the other comparisons.

Figure 3 shows the line profiles at the end of the hepatobiliary bile ducts and the gallbladder. The representative positions of the line profile are indicated by the red and green arrows in Figure 1(a), and the same position applies to respective reconstructions. The line profiles of SV are very close to the ground truth (GRAPPA) and show the highest PPCMM scores of 0.988 and 0.999 for Figure 3(a) and Figure 3(b), respectively. The blue arrows in Figure 3(a) demonstrate that both SV and SSV effectively remove aliasing artifacts, while the other reconstructions fail to do so. In addition, DL reconstructions preserve the image intensity of the gallbladder as well as GRAPPA x2 (see the pink circle in Figure 3(b)).

### Prospective study

Table 1 includes the required breathing cycles and actual acquisition time (TA). For MRCP acquisitions at R=2, 3T and 0.55T require 97 and 82 breathing cycles, respectively, corresponding to estimate times of 303 and 249 seconds. In contrast, acquisitions at R=6 for both field strengths require only 39 and 38 cycles, with corresponding times of 138 and 139 seconds. A similar tendency is seen for TA, where the average TAs at R=2 are 599 and 542 seconds for 3T and 0.55T, respectively, while at R=6, they are 255 and 180 seconds.

Figure 4 depicts the results of reconstructions for prospective undersampling with  $R=6$  for 3T and 0.55T. Only DL reconstructions clearly remove aliasing artifacts, as shown in the blue circles of Figure 4(a). In addition, DL reconstructions preserve the sharpness of the common bile ducts, while other reconstructions blur this area, as indicated by the orange circles in Figure 4(a). In the turquoise circles of Figure 4(b), fine hepatobiliary ducts, which are buried under the noise level in conventional reconstructions, become visible in the SV and SSV reconstructions.

## Discussion

The goal of our study was to reduce the acquisition time for PACE-using higher acceleration factors enabled by DL-based image reconstruction. We achieved accelerated PACE-MRCP acquisitions by undersampling three times more than in clinical applications, i.e., increasing the acceleration factor from  $R=2$  to  $R=6$ . Specifically, the TAs at  $R=6$  were 2.4 and 3.0 times faster than those at  $R=2$  for 3T and 0.55T, respectively. At the same time, the DL reconstructions alleviated the side effects such as aliasing artifacts and noise amplification caused by undersampling with high acceleration factors. Our prospective experiments demonstrate that DL reconstructions can be applied in real-world applications beyond retrospective simulations.

It is important to note that accelerating the MRCP acquisition was done only along the phase encoding direction. In other words, we performed experiments on a stack of 2-D data by fully sampling  $k$ -space data along the slice direction. As this was a preliminary study, we aimed to keep the study setup as simple as possible. However, this study could be extended to 3-D reconstruction, given that 3-D reconstructions have shown several benefits.

The t-Test between CS and SV, as illustrated in Table 2, reveals that only SSIM at 0.55T is statistically significant. However, Figure 1 and Figure 4 demonstrate that SV consistently produces superior image quality in terms of aliasing artifacts, background noise level, and sharpness. This indicates that the metric scores for MRCP do not fully reflect the actual image quality. One potential explanation for this discrepancy is that all metric scores are calculated with GRAPPA x2, which is not an ideal ground truth. Given that GRAPPA x2 is already subject to some degree of noise amplification and that the majority of MRCP slices are characterized by significant background noise, quantifying MRCP image quality using metrics such as PSNR and SSIM is challenging [30]. Therefore, though metric scores can provide some quantitative guidance, it is important to prioritize image quality and avoid over-interpreting these quantitative metric scores.

In addition, the results of supervised training using GRAPPA x2 consistently demonstrated higher quantitative metric scores compared to self-supervised training directly on the undersampled data. However, this is expected, as SV was trained to minimize differences between the output of the model and GRAPPA x2, whereas SSV was trained by itself. Given that the image quality of SV and SSV appears similar in Figure 1 and Figure 4, the focus should be on the visual quality of the reconstructions rather than on metric scores.

An interesting finding of our experiments is that, despite the ground truth for SV training not being fully sampled, SV performs as well as SSV. One possible explanation for this is that the acceleration factor used for our parallel imaging ground truth reconstructions followed the standard clinical MRCP protocol, which involved a relatively low value ( $R=2$ ). Consequently, our GRAPPA reconstructions yielded clinically acceptable image quality without significant artifacts or noise amplification.



One open question in the field of deep learning MR image reconstruction is the generalization of a single model with respect to changes in the image acquisition setup. In our experimental design, we tested this by training our deep learning model on 3T data and then applying it to data acquired at 0.55T. Our results show that even with this domain shift between training and testing, the data-driven deep learning models consistently outperformed compressed sensing and parallel imaging.

## Conclusion

We have achieved a significant reduction in acquisition time for PACE-MRCP with DL reconstruction. Our results demonstrate superior performance compared to conventional reconstructions, such as parallel imaging and compressed sensing, for both retrospectively and prospectively accelerated acquisitions, as well as generalizability across field strengths from 3T to 0.55T.

## Acknowledgements

This work is supported by the Erlangen National High Performance Computing Center (NHR@FAU) of Friedrich-Alexander-Universität Erlangen-Nürnberg (FAU) under the NHR project b143dc. NHR funding is provided by federal and Bavarian state authorities. NHR@FAU hardware is partially funded by the German Research Foundation (DFG) – 440719683. The authors thank Thomas Benkert, Bruno Riemenschneider, Zhengguo Tan, and Marc Vornehm for the beneficial discussion and technical supports.

## Conflict of Interest Statement

J.K. receives a PhD stipend from Siemens Healthineers AG. M.D.N. is employed by Siemens Healthineers AG. F.K. receives research support from Siemens Healthineers AG, has stock options from Subtle Medical and is a consultant for Imaginostics.

## Data Availability Statement

The Python implementations of the reconstruction framework with sample dataset are available to any interested researchers ([https://github.com/JinhoKim46/MRCP\\_DLRecon](https://github.com/JinhoKim46/MRCP_DLRecon)).

## Funding Information

DFG, Grant/Award Number: 513220538; NIH, Grant/Award Number: R01EB024532, P41EB017183

## Abbreviations

MRCP, magnetic resonance cholangiopancreatography; DL, deep learning; SV, supervised training; SSV, self-supervised training; SSDU, self-supervised learning via data undersampling; PI, parallel imaging; CG-SENSE, conjugate gradient sensitivity encoding imaging; CS, compressed sensing imaging; FID, free induction decay; IFT, inverse Fourier transform; PACE, prospective acquisition correction technique; MIP, maximum intensity projection; PPMCC, Pearson product-moment correlation coefficient, PSNR, peak signal-to-noise ratio; SSIM, structural similarity; SNR, signal-to-noise ratio;

## Figures

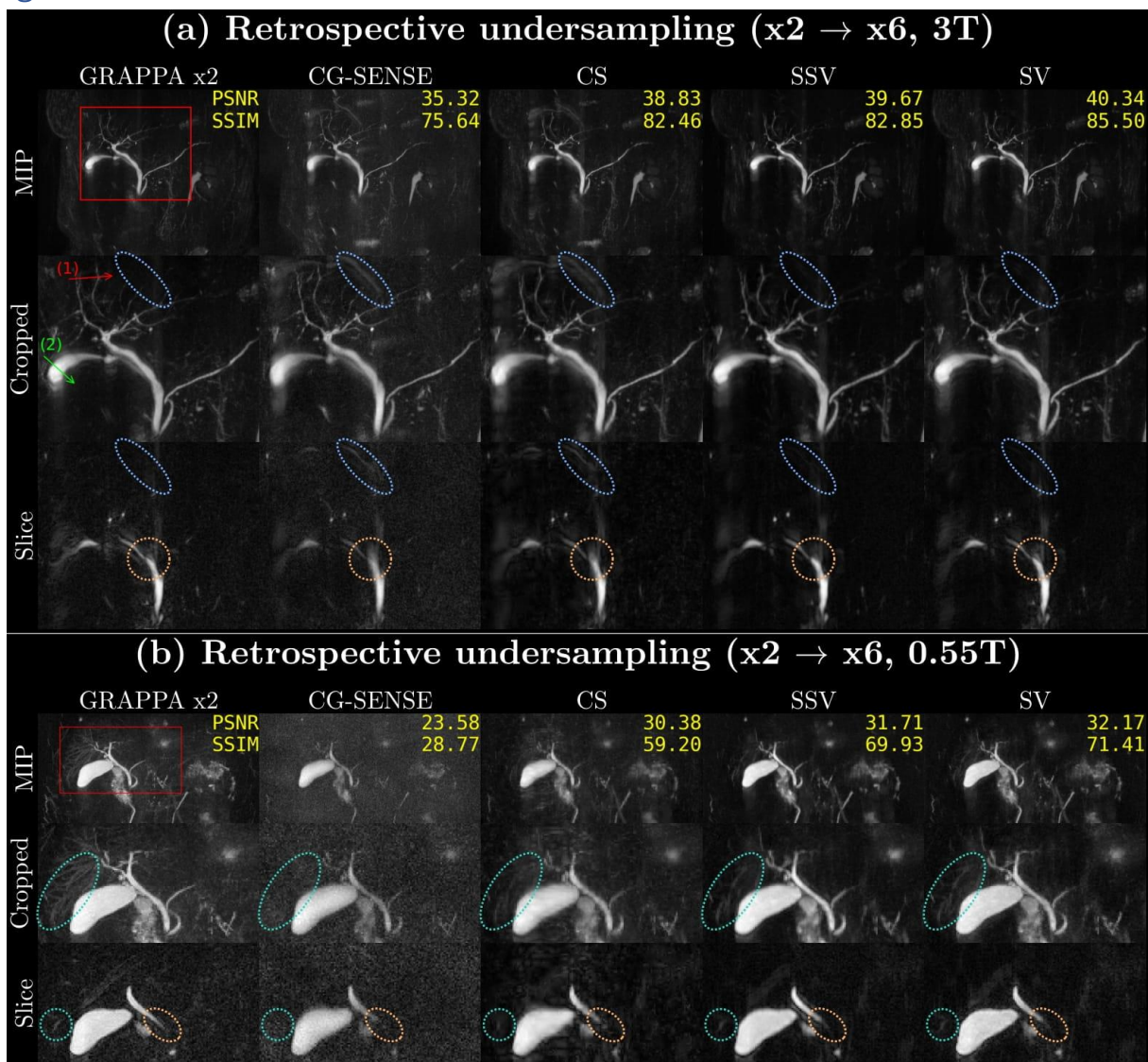


Figure 1: Results of retrospective undersampling at (a) 3T and (b) 0.55T: We use GRAPPA with two-fold acceleration as the ground truth for comparison with CG-SENSE, CS, SSV, and SV reconstructions with six-fold acceleration. Each column corresponds to a reconstruction method and shows three different presentation forms: Maximum Intensity Projection (MIP) (top), a cropped view of the hepatobiliary duct of the MIP (middle), and a representative single slice (bottom). In (a), the blue circles indicate aliasing artifacts, and the orange circles display the representative sharpness of the common bile duct. In (b), the turquoise circles show delicate details of the hepatobiliary ducts. The MIP images of the six-fold reconstructions are quantitatively assessed with PSNR in dB and SSIM in % with respect to GRAPPA  $x2$ . The red and green arrows in (a) indicate the signal intensity source for the line profile representation for Figure 3.

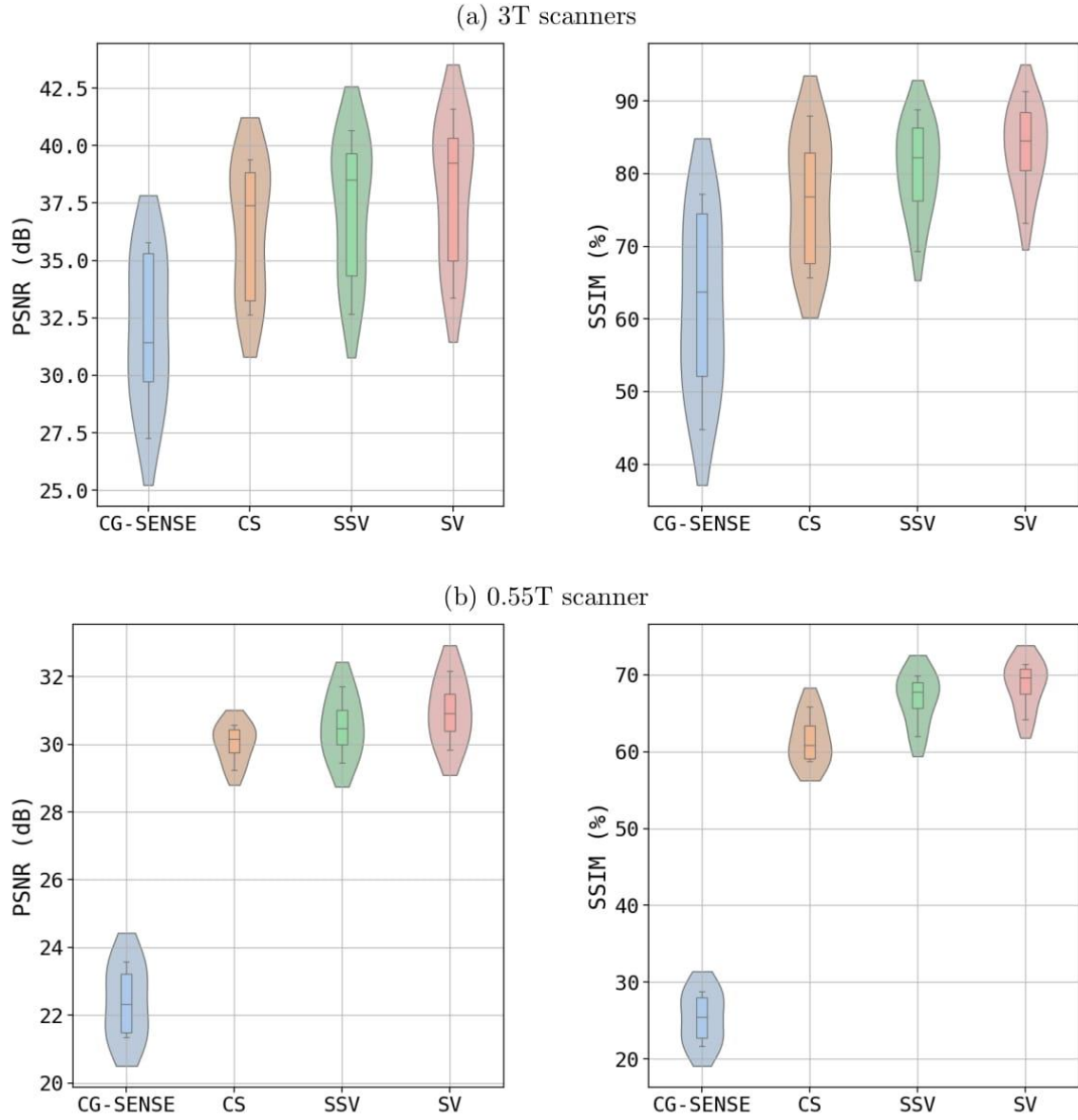


Figure 2: Violin plots of PSNR in dB and SSIM in % of the different reconstruction methods against the R=2 GRAPPA reconstructions for (a) 3T (nine test set subjects) and (b) 0.55T (four test set subjects). Within each graph, box plots are included to provide a visual representation of the data distribution range.

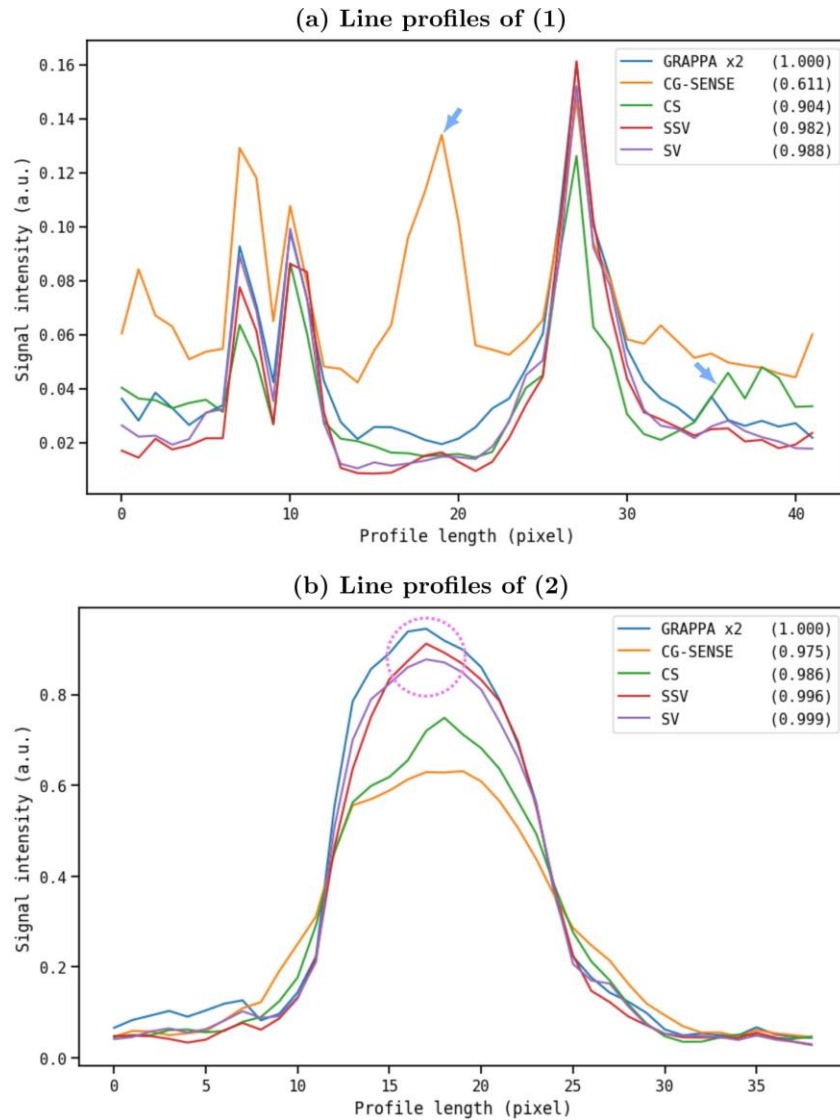


Figure 3: Line profiles from the retrospective study. The line profiles are taken from the same position of the corresponding reconstructions, respectively, and one representative position is presented as the red arrow (a) and the green arrow (b) in Figure 1(a). Pearson product-moment correlation coefficients (PPMCC) against GRAPPA x2 are shown in the legend for the corresponding reconstructions to quantify the similarity to the reference profile. SV presents the highest PPMCC among others, meaning that the line profile of SV is the most similar to GRAPPA x2. The blue arrows in (a) indicates aliasing artifacts of CG-SENSE and CG. The pink circle in (b) demonstrates that DL reconstructions preserve signal intensity of the gallbladder.

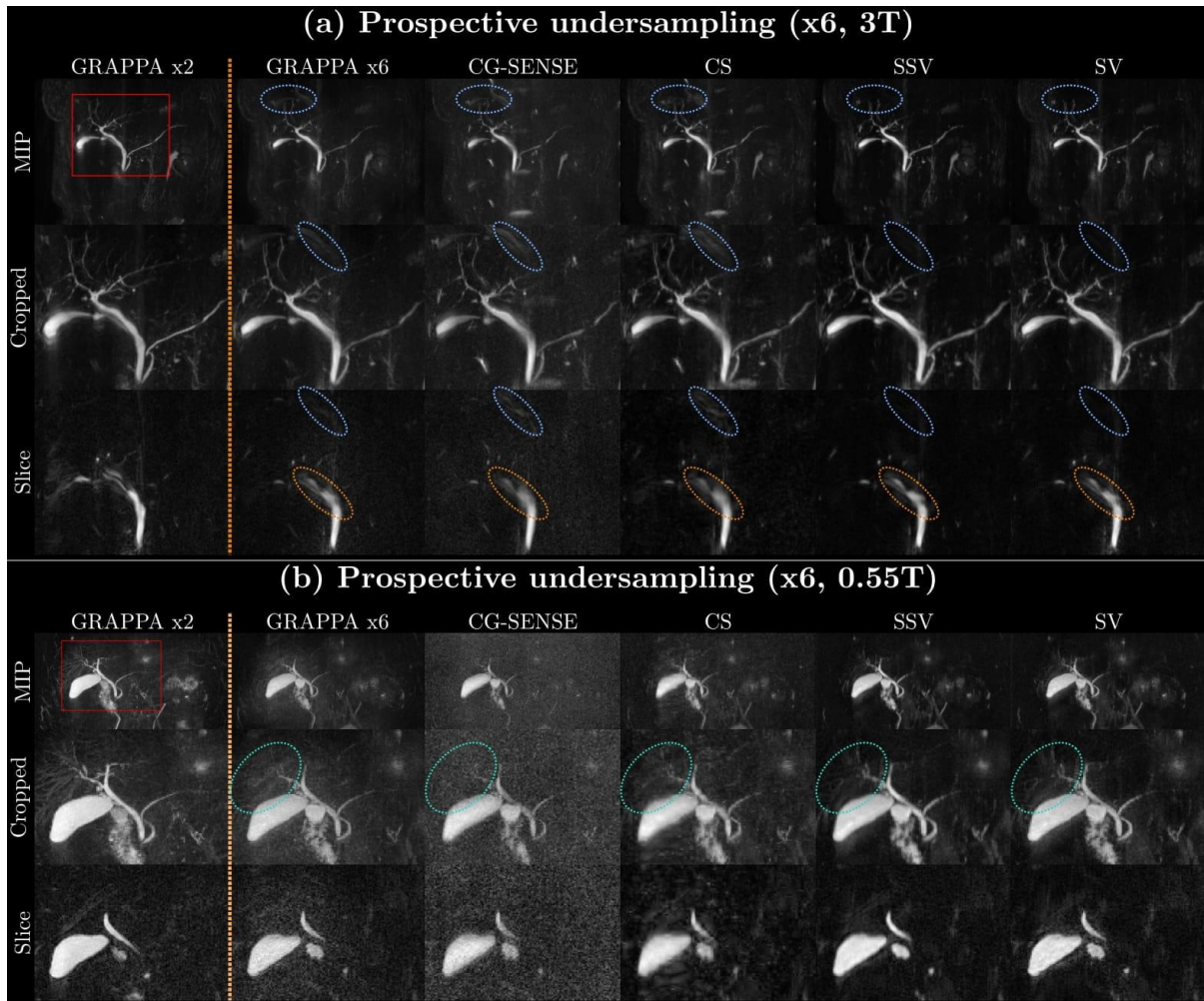


Figure 4: Results of prospective undersampling at (a) 3T and (b) 0.55T: We use GRAPPA with a two-fold acceleration to serve as a reference (GRAPPA x2). Then we reconstruct six-fold accelerated acquisitions using GRAPPA x6, CG-SENSE, CS, SSV, and SV approaches. Each column corresponds to one reconstruction method and shows three different presentation forms: Maximum Intensity Projection (MIP) (top), a cropped view of the hepatobiliary duct of the MIP (middle), and a representative single slice (bottom). In (a), the blue circles indicate aliasing artifacts, and the orange circles represent the sharpness of the anatomical regions. In (b), the turquoise circles show delicate details of the hepatobiliary ducts.

## Tables

Table 1: Parameters for MRI protocols

Parameters	3T		0.55T	
Scanner	MAGNETOM Vida & Lumina		MAGNETOM Free.Max	
Sequence	3-D T2-weighted TSE (SPACE) [20]			
Acquisition plane	Coronal			
Turbo factor	180			
TR (ms)*	5985 ± 2103 (2700–12829)		5298 ± 1462 (4251–8878)	
TE (ms)*	703 ± 2 (701–709)		703	
Acquired voxel size (mm <sup>3</sup> )	0.5 × 0.5 × 1.2		0.7 × 0.7 × 1.0	
Matrix	384 × 480		256 × 194	
Number of slices			64	
Flip angles*	115, 120		145	
Echo train spacing (ms)	5.26		5.58	
Echo train duration (ms)	957		1016	
Number of signal averages	1.4		2	
Bandwidth (Hz/pixel)	352		391	
Triggering	PACE signal			
Number of ACS lines	24			
Parallel imaging acceleration PE	x2	x6	x2	x6
Parallel imaging acceleration 3D	x1			
Breathing cycles (estim. time (s))	97 (303)	39 (138)	82 (249)	38 (139)
TA (s)*	599 ± 283 (229–1386)	255 ± 81 (161–426)	542 ± 172 (370–720)	180 ± 28 (158–226)

TSE, turbo spin-echo; TR, repetition time; TE, echo time; ACS, autocalibration signal; PE, phase encoding; TA, acquisition time; estim. time, estimated time.

The notation format for TR, TE, and TA is Mean ± Standard deviation (Minimum – Maximum).

\* Variable depending on the volunteer.

Table 2: Quantitative analysis of the retrospective study at R=6

		CG-SENSE	CS	SSV	SV	<i>p</i> -value		
						CG-SENSE vs. SV	CS vs. SV	SSV vs. SV
3T	PSNR	32.05 ± 3.01	36.44 ± 2.69	37.29 ± 2.79	<b>38.02 ± 2.81</b>	< 0.001*	0.269	0.607
	SSIM	62.08 ± 11.22	76.52 ± 8.06	80.79 ± 5.88	<b>83.63 ± 5.38</b>	< 0.001*	0.054	0.329
0.55T	PSNR	22.39 ± 0.97	30.03 ± 0.51	30.53 ± 0.82	<b>30.96 ± 0.86</b>	< 0.001*	0.158	0.556
	SSIM	25.34 ± 3.0	61.58 ± 2.85	66.9 ± 3.01	<b>68.72 ± 2.77</b>	< 0.001*	0.020*	0.410

CG-SENSE, conjugate gradient SENSE; CS, compressed sensing; SSV, self-supervised model; VN, supervised model; PSNR, peak signal-to-noise ratio; SSIM, structural similarity.

The notation format for PSNR and SSIM is Mean ± Standard deviation.

PSNR and SSIM are averaged over nine test data for 3T and four for 0.55T.

\* *p*-value < 0.05 is considered statistically significant.

## References

- [1] M. A. Barish, E. K. Yucel and J. T. Ferrucci, "Magnetic resonance cholangiopancreatography," *New England Journal of Medicine*, vol. 341, no. 4, pp. 258-264, 1999.
- [2] H. Irie, H. Honda, T. Tajima, T. Kuroiwa, K. Yoshimitsu, K. Makisumi and K. Masuda, "Optimal MR cholangiopancreatographic sequence and its clinical application," *Radiology*, vol. 206, no. 2, pp. 379-387, 1998.
- [3] A. S. Fulcher, M. A. Turner and G. W. Capps, "MR Cholangiography: Technical Advances and Clinical Applications," *Radiographics*, vol. 19, no. 1, pp. 25-44, 1999.
- [4] S. Nagata, S. Goshima, Y. Noda, N. Kawai, K. Kajita, H. Kawada, Y. Tanahashi and M. Matsuo, "Possible biliary disease: Diagnostic performance of high-spatial-resolution isotropic 3D T2-weighted MRCP," *Radiology*, vol. 249, no. 3, pp. 883-890, 2008.
- [5] L. S. Yoon, O. A. Catalano, S. Fritz, C. R. Ferrone, P. F. Hahn and D. V. Sahani, "Another Dimension in Magnetic Resonance Cholangiopancreatography: Comparison of 2-and 3-Dimensional Magnetic Resonance Cholangiopancreatography for the Evaluation of Intraductal Papillary Mucinous Neoplasm of the Pancreas," *Journal of computer assisted tomography*, vol. 33, no. 3, pp. 363-368, 2009.
- [6] S. Morita, E. Ueno, K. Suzuki, H. Machida, M. Fujimura, S. Kojima, M. Hirata, T. Ohnishi and C. Imura, "Navigator-triggered prospective acquisition correction (PACE) technique vs. conventional respiratory-triggered technique for free-breathing 3D MRCP: An initial prospective comparative study using healthy volunteers," *Journal of Magnetic Resonance Imaging: An Official Journal of the International Society for Magnetic Resonance in Medicine*, vol. 28, no. 3, pp. 679-677, 2008.
- [7] P. Asbach, C. Klessen, T. J. Kroencke, C. Kluner, A. Stemmer, B. Hamm and M. Taupitz, "Magnetic resonance cholangiopancreatography using a free-breathing T2-weighted turbo spin-echo sequence with navigator-triggered prospective acquisition correction," *Magnetic resonance imaging*, vol. 23, no. 9, pp. 939-945, 2005.
- [8] B. Sun, Z. Chen, Q. Duan, Y. Xue, E. Zheng, Y. He, L. Lin, G. Li and Z. Zhang, "Rapid 3D navigator-triggered MR cholangiopancreatography with SPACE sequence at 3T: only one-third acquisition time of conventional 3D SPACE navigator-triggered MRCP," *Abdominal Radiology*, vol. 45, no. 1, pp. 134-140, 2020.
- [9] S. Nagata, S. Goshima, Y. Noda, N. Kawai, K. Kajita, H. Kawada, Y. Tanahashi and M. Matsuo, "Magnetic resonance cholangiopancreatography using optimized integrated combination with parallel imaging and compressed sensing technique," *Abdominal Radiology*, vol. 44, pp. 1766-1772, 2019.
- [10] J. H. Yoon, S. M. Lee, H. J. Kang, E. Weiland, E. Raithel, Y. Son, B. Kiefer and J. M. Lee, "Clinical Feasibility of 3-Dimensional Magnetic Resonance Cholangiopancreatography Using Compressed



- Sensing: Comparison of Image Quality and Diagnostic Performance," *Investigative radiology*, vol. 52, no. 10, pp. 612-619, 2017.
- [11] K. P. Pruessmann, M. Weiger, M. B. Scheidegger and P. Boesiger, "SENSE: Sensitivity encoding for fast MRI," *Magnetic Resonance in Medicine: An Official Journal of the International Society for Magnetic Resonance in Medicine*, vol. 42, no. 5, pp. 952-962, 1999.
- [12] M. Lustig, D. Donoho and J. M. Pauly, "Sparse MRI: The application of compressed sensing for rapid MR imaging," *Magnetic Resonance in Medicine: An Official Journal of the International Society for Magnetic Resonance in Medicine*, vol. 58, no. 6, pp. 1182-1195, 2007.
- [13] C. M. Hyun, H. P. Kim, S. M. Lee, S. Lee and J. K. Seo, "Deep learning for undersampled MRI reconstruction," *Physics in Medicine & Biology*, vol. 63, no. 13, p. 135007, 2018.
- [14] H. K. Aggarwal, M. P. Mani and M. Jacob, "MoDL: Model-Based Deep Learning Architecture for Inverse Problems," 2019.
- [15] B. Yaman, S. A. H. Hosseini, S. Moeller, J. Ellermann, K. Uğurbil and M. Akçakaya, "Self-supervised learning of physics-guided reconstruction neural networks without fully sampled reference data," *Magnetic resonance in medicine*, vol. 84, no. 6, pp. 3172-3191, 2020.
- [16] F. Knoll, K. Hammernik, E. Kobler and D. K. Sodickson, "Assessment of the generalization of learned image reconstruction and the potential for transfer learning," *Magnetic resonance in medicine*, vol. 81, no. 1, pp. 116-128, 2019.
- [17] J. P. Marques, F. F. Simonis and A. G. Webb, "Low-field MRI: An MR physics perspective," *Journal of magnetic resonance imaging*, vol. 49, no. 6, pp. 1528-1542, 2019.
- [18] M. Akçakaya, S. Nam, P. Hu, M. H. Moghari, L. H. Ngo, V. Tarokh, W. J. Manning and R. Nezafat, "Compressed sensing with wavelet domain dependencies for coronary MRI: A retrospective study," *IEEE Transactions on Medical Imaging*, vol. 30, no. 5, pp. 1090-1099, 2011.
- [19] K. P. Pruessmann, M. Weiger, P. Börnert and P. Boesiger, "Advances in sensitivity encoding with arbitrary k-space trajectories," *Magnetic Resonance in Medicine: An Official Journal of the International Society for Magnetic Resonance in Medicine*, vol. 46, no. 4, pp. 638-651, 2001.
- [20] S. Diamond, V. Sitzmann, F. Heide and G. Wetzstein, "Unrolled optimization with deep priors," *arXiv preprint arXiv:1705.08041*, 2017.
- [21] M. A. Griswold, P. M. Jakob, R. M. Heidemann, M. Nittka, V. Jellus, J. Wang, B. Kiefer and A. Haase, "Generalized Autocalibrating Partially Parallel Acquisitions (GRAPPA)," *Magnetic Resonance in Medicine: An Official Journal of the International Society for Magnetic Resonance in Medicine*, vol. 47, no. 6, pp. 1202-1210, 2002.
- [22] M. P. Lichy, B. M. Wietek, J. P. Mugler Iii, W. Horger, Marion, I. Menzel, A. Anastasiadis, K. Siegmann, T. Niemyer, A. Königsrainer, B. Kiefer, F. Schick, C. D. Claussen and H.-P. Schlemmer, "Magnetic Resonance Imaging of the Body Trunk Using a Single-Slab, 3-Dimensional, T2-weighted

- Turbo-Spin-Echo Sequence With High Sampling Efficiency (SPACE) for High Spatial Resolution Imaging Initial Clinical Experiences," *Investigative Radiology*, vol. 40, pp. 756-760, 2005.
- [23] J. P. Mugler, "Optimized three-dimensional fast-spin-echo MRI," *Journal of Magnetic Resonance Imaging*, vol. 39, no. 4, pp. 745-767, 2014.
- [24] S. J. Inati, J. D. Naegele, N. R. Zwart, V. Roopchansingh, M. J. Lizak, D. C. Hansen, C.-Y. Liu, D. Atkinson, P. Kellman, S. Kozerke and others, "ISMRM Raw data format: A proposed standard for MRI raw datasets," *Magnetic resonance in medicine*, vol. 77, no. 1, pp. 411-421, 2017.
- [25] M. Uecker, P. Lai, M. J. Murphy, P. Virtue, M. Elad, J. M. Pauly, S. S. Vasanawala and M. Lustig, "ESPIRiT - An eigenvalue approach to autocalibrating parallel MRI: Where SENSE meets GRAPPA," *Magnetic resonance in medicine*, vol. 71, no. 3, pp. 990-1001, 2014.
- [26] F. Ong and M. Lustig, "SigPy: a python package for high performance iterative reconstruction," in *Proceedings of the ISMRM 27th Annual Meeting*, 2019.
- [27] K. He, X. Zhang, S. Ren and J. Sun, "Deep Residual Learning for Image Recognition," *Proceedings of the IEEE conference on computer vision and pattern recognition*, pp. 770-778, 2016.
- [28] C. Millard and M. Chiew, "A theoretical framework for self-supervised MR image reconstruction using sub-sampling via variable density Noisier2Noise," *IEEE transactions on computational imaging*, vol. 9, pp. 707-720, 2023.
- [29] K. Pearson, "Notes on the history of correlation," *Biometrika*, vol. 13, no. 1, pp. 25-45, 1920.
- [30] Wang, A. Jiayang, H. Di and J. P., "The "hidden noise" problem in MR image reconstruction," *Magnetic Resonance in Medicine*, vol. 92, no. 3, pp. 982-996, 2024.